

Storing quantum information for 30 seconds in a nanoelectronic device

Juha T. Muhonen^{1*}, Juan P. Dehollain¹, Arne Laucht¹, Fay E. Hudson¹, Rachpon Kalra¹, Takeharu Sekiguchi², Kohei M. Itoh², David N. Jamieson³, Jeffrey C. McCallum³, Andrew S. Dzurak¹ and Andrea Morello^{1*}

The spin of an electron or a nucleus in a semiconductor¹ naturally implements the unit of quantum information—the qubit. In addition, because semiconductors are currently used in the electronics industry, developing qubits in semiconductors would be a promising route to realize scalable quantum information devices². The solid-state environment, however, may provide deleterious interactions between the qubit and the nuclear spins of surrounding atoms³, or charge and spin fluctuations arising from defects in oxides and interfaces⁴. For materials such as silicon, enrichment of the spin-zero ²⁸Si isotope drastically reduces spin-bath decoherence⁵. Experiments on bulk spin ensembles in ²⁸Si crystals have indeed demonstrated extraordinary coherence times^{6–8}. However, it remained unclear whether these would persist at the single-spin level, in gated nanostructures near amorphous interfaces. Here, we present the coherent operation of individual ³¹P electron and nuclear spin qubits in a top-gated nanostructure, fabricated on an isotopically engineered ²⁸Si substrate. The ³¹P nuclear spin sets the new benchmark coherence time (>30 s with Carr–Purcell–Meiboom–Gill (CPMG) sequence) of any single qubit in the solid state and reaches >99.99% control fidelity. The electron spin CPMG coherence time exceeds 0.5 s, and detailed noise spectroscopy⁹ indicates that—contrary to widespread belief—it is not limited by the proximity to an interface. Instead, decoherence is probably dominated by thermal and magnetic noise external to the device, and is thus amenable to further improvement.

It is well known that the Si/SiO₂ interface hosts a variety of defects that act as charge and spin fluctuators. Experiments have documented the deleterious effects of the Si/SiO₂ interface on the coherence of donors in ²⁸Si (refs 10,11). Theoretical models suggest that the fluctuations of paramagnetic spins at the interface cause the decohering noise⁴, and recent work advocates the use of ‘clock transitions’ in ²⁰⁹Bi donors¹² to obtain a spin qubit that is, to first order, insensitive to magnetic noise. Fluctuations of interface charges or gate voltages can also cause decoherence, if there is a physical mechanism for electric fields to couple to the spin qubit states. Evidence of such effects has been found for instance in carbon nanotube valley-spin qubits¹³. For donors in silicon, fluctuating electric fields can couple to the spin states by modulating the hyperfine coupling¹⁴ or the electron *g*-factor¹⁵. Here, we operate single-atom spin qubits in isotopically purified ²⁸Si, with a residual ²⁹Si concentration of 800 ppm. Minimizing the effect of ²⁹Si nuclear spin fluctuations allows us not only to set new benchmarks for qubit performance in the solid state, but also to investigate the

microscopic origin of residual decoherence mechanisms, specific to a gated nanostructure.

A substitutional P atom in Si behaves to a good approximation like hydrogen in vacuum, with energy levels renormalized by the effective mass and the dielectric constant of the host material¹⁶. Both the bound electron (*e*[−]) and the nucleus (³¹P) possess a spin 1/2 and constitute natural qubits with simple spin-up/down eigenstates, which we denote as $|\uparrow\rangle, |\downarrow\rangle$ for *e*[−] and $|\uparrow\rangle, |\downarrow\rangle$ for ³¹P. The contact hyperfine interaction *A* between *e*[−] and ³¹P, and the application of a static magnetic field *B*₀ > 1 T result in a four-level energy diagram, as shown in Fig. 1c. At high magnetic fields the eigenstates are, to a very good approximation, the separable tensor products of the electro-nuclear basis states.

The device structure is shown in Fig. 1a,b. It consists of a silicon single-electron transistor (SET) for spin readout¹⁷, a broadband on-chip microwave antenna to deliver an oscillating magnetic field *B*₁ to the qubits¹⁸, ion-implanted P donors¹⁹, and a stack of aluminium gates above the SiO₂ insulator to control the potentials of the donors and the SET. The donors are expected to be at an average depth of ~10 nm below the Si/SiO₂ interface. All the data presented here are obtained from analysis of single-shot electron¹⁷ and nuclear²⁰ spin readout events. We have measured two devices, A and B, which differ slightly in their gate layout and ion-implantation parameters (see Methods). The experiments were performed in high magnetic fields (*B*₀ = 1.62 T for device A, *B*₀ = 1.5 T for device B) and low temperatures (electron temperature *T*_e ≈ 100 mK). The two devices had significantly different hyperfine constants (*A*/*h* ≈ 116.6 MHz for device A and 96.9 MHz for device B), probably resulting from a combination of different donor depths, electric fields¹⁴ or strain.

We report a complete set of qubit control and coherence benchmarks, including (1) Rabi oscillations, to prepare arbitrary superposition states of the qubit; (2) Ramsey fringes, which yield the pure dephasing time *T*₂^{*}; (3) Hahn echoes, which yield the qubit coherence time *T*₂^H; (4) Carr–Purcell–Meiboom–Gill (CPMG_N) dynamical decoupling sequences, used here both to extend the coherence time *T*₂^{CPMG} and to extract the spectrum of the noise that couples to the qubits (for more details see Supplementary Section B).

The coherent operation of the *e*[−] qubit is shown in Fig. 2a. The Rabi oscillations continue for over 500 μs before any signs of decay (only the first 100 μs are shown). This is a tremendous improvement over the *e*[−] qubit in ^{nat}Si, where the Rabi oscillations decayed in less than 1 μs (ref. 21). The Ramsey experiment (Fig. 2b) yields an electron pure dephasing time *T*_{2e}^{*} = 270 μs on device A, a 5,000-fold improvement over the ^{nat}Si value of 55 ns (ref. 21) and comparable to the values obtained with nitrogen-vacancy (NV) electron spins in

¹Centre for Quantum Computation and Communication Technology, School of Electrical Engineering and Telecommunications, UNSW Australia, Sydney, New South Wales 2052, Australia, ²School of Fundamental Science and Technology, Keio University, 3-14-1 Hiyoshi, 223-8522, Japan, ³Centre for Quantum Computation and Communication Technology, School of Physics, University of Melbourne, Melbourne, Victoria 3010, Australia.

*e-mail: juha.muhonen@unsw.edu.au; a.morello@unsw.edu.au

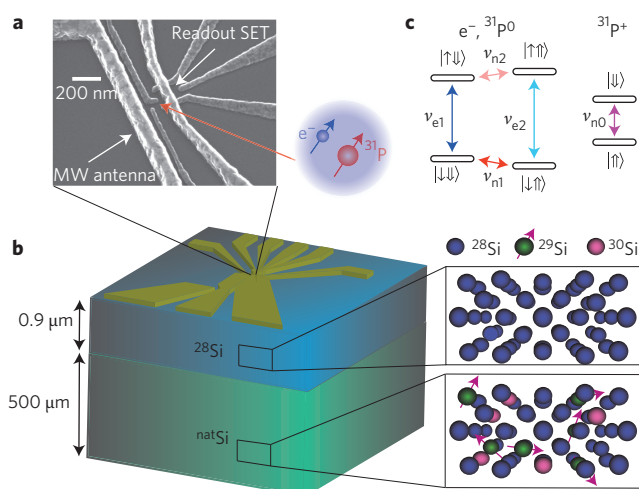


Figure 1 | Device structure and the energy states of the electron and nuclear spin qubits. **a**, Scanning electron micrograph image of a device similar to device A, highlighting the position of the P donor, the microwave (MW) antenna and the SET for spin readout. **b**, Schematic of the Si substrate, consisting of an isotopically purified ^{28}Si epilayer (with a residual ^{29}Si concentration of 800 ppm) on top of a natural Si wafer. **c**, Energy level diagram of the coupled $e^- - ^{31}\text{P}^0$ system (left) and the ionized $^{31}\text{P}^+$ nucleus (right). Arbitrary quantum states are encoded on the qubits by applying pulses of oscillating magnetic field B_1 at the frequencies corresponding to the ESR ($\nu_{e1,2} \approx \gamma_e B_0 \mp A/2$) and NMR ($\nu_{n1,2} \approx A/2 \pm \gamma_n B_0$), where $\gamma_e = 27.97 \text{ GHz T}^{-1}$ and $\gamma_n = 17.23 \text{ MHz T}^{-1}$ are the electron and nuclear gyromagnetic ratios, respectively. The ^{31}P qubit in the ionized state is operated at frequency $\nu_{n0} = \gamma_n B_0$.

isotopically purified ^{12}C diamond^{22,23}. The Ramsey envelope decay is Gaussian. The electron spin resonance (ESR) line is extremely sharp, and measuring it directly requires the use of low-power, shaped (Gaussian) pulses. In device B we observed a full-width at half-maximum (FWHM) of 1.8 kHz (Fig. 2c), in good agreement with $T_{2e}^* = 160 \mu\text{s}$. With a Hahn-echo sequence we measured electron coherence times $T_{2e}^H \approx 1 \text{ ms}$ in both devices (Fig. 2d), only a factor of 5 longer than in $^{\text{nat}}\text{Si}$ (ref. 21). However, using the CPMG dynamical decoupling technique we further extended the e^- spin coherence, reaching $T_{2e}^{\text{CPMG}} = 0.56 \text{ s}$ in device B (Fig. 2e).

For the ^{31}P qubit we report coherence measurements in the neutral ($^{31}\text{P}^0$) and the ionized ($^{31}\text{P}^+$) case (Fig. 3). The $^{31}\text{P}^0$ shows a similar dephasing time to e^- , $T_{2n0}^* \approx 500 \mu\text{s}$ (Fig. 3a, left). The Hahn-echo decay was found to be very different in devices A and B, with values of 1.5 ms and 20 ms, respectively (Fig. 3b, left). For the neutral nucleus, applying a CPMG sequence did not extend the coherence time (Fig. 3c, left). The details of the decoherence processes acting on the neutral nucleus are currently not understood. However, as observed previously in both single-atom²⁰ and bulk experiments⁸, the nuclear spin coherence improves dramatically by removing the electron from the P atom. The donor ionization is performed electrically, by raising the donor potential above the Fermi level of the nearby charge reservoir and forcing the donor-bound electron to tunnel out²⁰. The $^{31}\text{P}^+$ Ramsey decay times reached the value $T_{2n+}^* = 0.6 \text{ s}$ in device B (Fig. 3a, right), which would correspond to an NMR linewidth of $\Delta\nu_{\text{FWHM}} \approx 0.4 \text{ Hz}$. The simple Hahn-echo sequence preserves the qubit coherence beyond 1 s, $T_{2n+}^H = 1.75 \text{ s}$ (Fig. 3b, right), and the CPMG dynamical decoupling extends it beyond 30 s, $T_{2n+}^{\text{CPMG}} = 35.6 \text{ s}$ in device B (Fig. 3c, right). This currently represents the record coherence for any single qubit in the solid state. A summary of the coherence benchmarks for e^- , $^{31}\text{P}^0$ and $^{31}\text{P}^+$ in both devices is provided in Supplementary Section A. The coherence decay exponent n is

larger than 1 in all measurements, resulting in an enhanced quantum state preservation at short times.

The qubit measurement fidelities F_m were extracted from high-resolution Rabi oscillation measurements (Supplementary Section D), using a method developed in earlier work^{20,21}. For the e^- qubit, F_m is limited by the interplay of measurement bandwidth and electron tunnel times¹⁷ and by the occurrence of false spin-up counts due to thermal effects. Through careful filtering of the signal lines we reduced the electron temperature to $\sim 100 \text{ mK}$ and achieved a measurement fidelity of $F_m \approx 97\%$. For the ^{31}P qubit, the readout fidelity depends on the ratio between the readout time and the average time between spin flips²⁰. Here, we achieved $F_m \approx 99.995\%$.

The use of isotopically purified ^{28}Si brought a dramatic improvement in the qubit control fidelities. In $^{\text{nat}}\text{Si}$, the e^- control fidelity was limited to $F_c = 57\%$ (ref. 21) by the randomness of the instantaneous resonance frequency, which fluctuated over a range comparable to the spectral width of the control pulse. Here, the ESR linewidth is instead two orders of magnitude smaller than the excitation pulse spectrum, which would yield an intrinsic control fidelity of order 99.9999%. Accordingly, the control errors arise solely from variation in pulse parameters due to the technical limitations of the room-temperature electronic set-up. For the specific case of a π -pulse around one axis, the control errors can be estimated by comparing the coherence decay obtained from CPMG, which is insensitive to pulse errors up to fourth order and from Carr-Purcell (CP), where the errors accumulate²⁴. With this method we obtained effective control fidelities $F_c^e \approx 99.6\%$ for e^- , 99.9% for $^{31}\text{P}^0$ and 99.99% for $^{31}\text{P}^+$ (for data plots see Supplementary Section D). Future work will focus on benchmarking complete sets of single-qubit gates.

Despite the record coherence times discussed above, our results do not match those obtained in bulk ensembles^{6–8}. We investigate the microscopic origin of spin decoherence by performing a systematic analysis of the spectral properties of the noise power $S(\omega)$ that modulates the e^- qubit energy splitting. We concentrate our analysis on the electron spin, because it is the most sensitive to both magnetic and electric field noise. We adopt a noise spectroscopy method based on the properties of CPMG sequences, which act as a bandpass filter for the noise^{25,26} with passband frequency centred at $\omega_p = \pi/\tau$, where τ is the delay between the π -pulses (Supplementary Section E). Therefore, by choosing different τ we shift the centre frequency of the filter, that is, which portion of the noise spectrum couples to the qubit. The benefits of dynamical decoupling are easily understood by considering a coloured noise, for example, $S(\omega) \propto 1/\omega$. Adding more π -pulses, thus reducing τ , shifts ω_p to a higher frequency where the noise is weaker. For the same reason, dynamical decoupling is ineffective in the presence of frequency-independent (white) noise.

In Fig. 4a we show $S(\omega)$ extracted using the method described in ref. 9, which accounts for the higher harmonics in the CPMG filter function, giving small corrections to the simple relation $S(\omega_p) = \pi^2/(4T_2^S)$ that would hold when considering the first harmonic only (simple bandpass filter). Here, T_2^S is the electron coherence time measured while keeping τ constant and progressively increasing the number of pulses in a CPMG sequence. At frequencies $\omega/2\pi > 3 \text{ kHz}$ the noise spectrum appears flat, $S(\omega) \approx 10 \text{ (rad s}^{-1}\text{)}^2 \text{ Hz}^{-1}$ in device A, corresponding to $T_2^S \approx 0.2 \text{ s}$. (For white noise, summing all the harmonics of the filter function leads to $S(\omega) = 2/T_2^S$.) Assuming that the noise is of magnetic origin, this corresponds to a longitudinal magnetic field noise of $b_n = \hbar \sqrt{S(\omega)}/(g\mu_B) = 18 \text{ pT Hz}^{-1/2}$. It is interesting to notice that substituting the simple bandpass formula here, we would recover the equation for sensitivity obtained by viewing the e^- qubit as an a.c. magnetic field sensor $\eta_{\text{a.c.}} = \pi\hbar/(2g\mu_B\sqrt{T_2})$ (ref. 27).

A plausible source of white noise is thermal Johnson–Nyquist radiation, coupling to the electron spin through the microwave

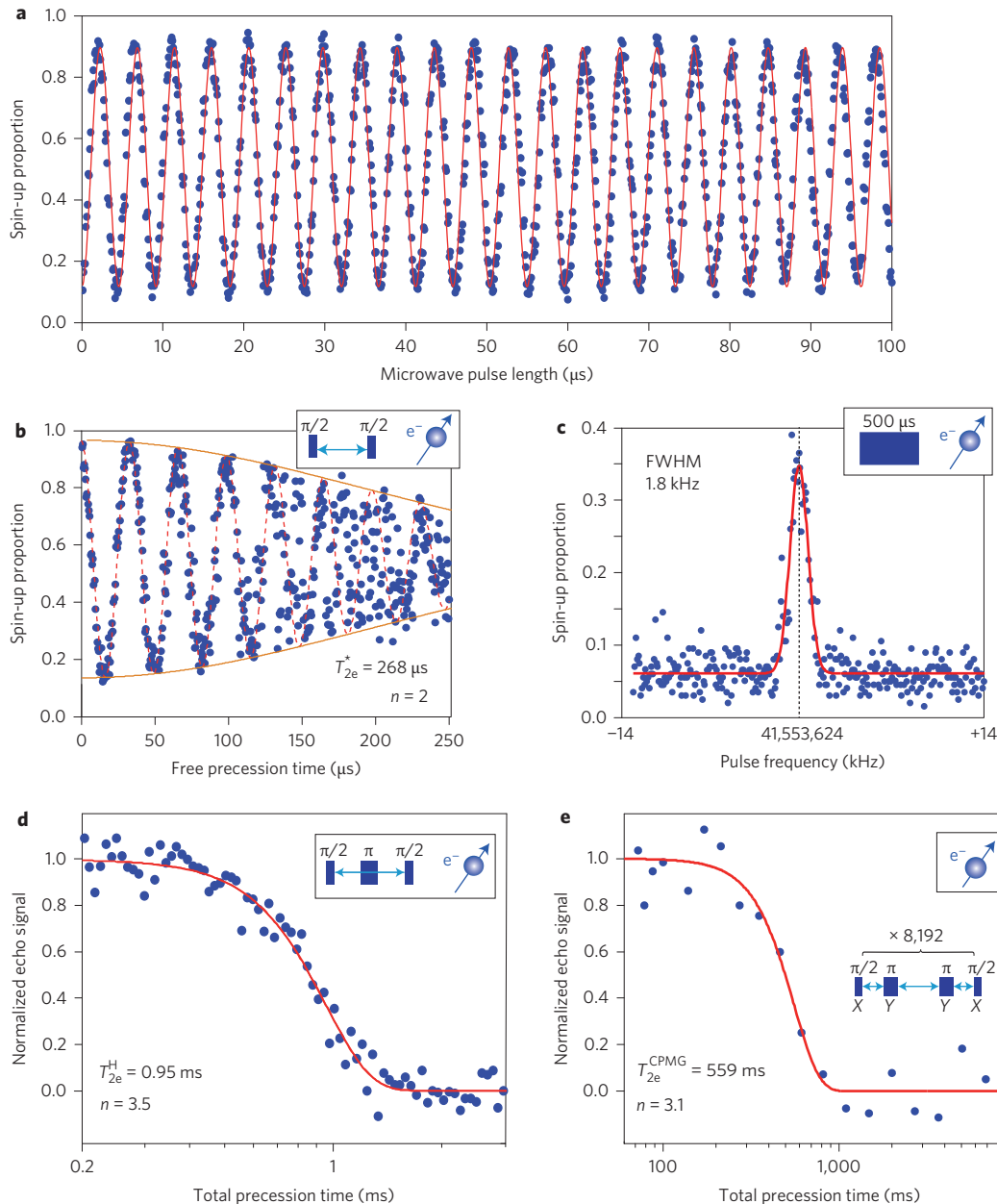


Figure 2 | Electron spin qubit. **a**, Long-lasting Rabi oscillations of the e^- qubit. **b**, e^- Ramsey fringes, showing a Gaussian decay envelope. **c**, ESR spectrum. The fit is a Gaussian function with FWHM = 1.8 kHz. **d**, e^- Hahn-echo decay. **e**, CPMG dynamical decoupling decay. The number of pairs of π -pulses is indicated in the inset. X and Y indicate the axes around which the spin is rotated, through the application of microwave pulses in-phase (X) or in-quadrature (Y) with the reference clock. The coherence times quoted in each panel are obtained by fitting the decays with functions of the form $P_0 \exp(-(t/T_2)^n) + P_\infty$. The decay exponent n is related to the frequency dependence of the power spectral density $S(\omega)$ of the noise that couples to the qubit (Supplementary Section E). The Hahn-echo and CPMG plots are normalized with respect to P_0 and P_∞ . Data in **c** and **e** are from device B; all other data are from device A.

antenna. Through finite-elements modelling of the magnetic field produced by the antenna at the qubit location (Supplementary Section F), we calculate that the observed noise amplitude would correspond to the Johnson–Nyquist noise produced by a 76 Ω resistor at 300 K. This is remarkably close to the 50 Ω output impedance of the microwave source. Before cooling device B, we added a further 7 dB attenuation at the 1.5 K stage of the dilution refrigerator, to reduce the amount of room-temperature thermal radiation that reaches the qubit. Device B indeed exhibited a reduced white-noise floor, $S(\omega) \approx 6 \text{ (rad s}^{-1}\text{)}^2 \text{ Hz}^{-1}$ and $b_n = 14 \text{ pT Hz}^{-1/2}$, albeit not by the exact amount expected on the basis of the additional attenuation. This could be due to a different location of the donor with respect to the antenna.

Both devices exhibit a coloured noise spectrum of nearly identical strength below 3 kHz, approximately $S(\omega) \propto 1/\omega^{2.5}$ (Fig. 4a,b). This coloured noise impacts the Ramsey T_{2e}^* and Hahn-echo T_{2e}^H coherence times in particular. The power-law of the noise is confirmed by the fact that the coherence times obtained as a function of the number N of refocusing pulses agree with the predicted scaling $T_{2e}^{\text{CPMG}} \propto N^{\alpha/(\alpha+1)}$, where $\alpha = 2.5$ (Fig. 4b)²⁸. Several microscopic mechanisms could be responsible for this noise, most of which can be ruled out quantitatively or qualitatively.

First, we rule out magnetic noise from other paramagnetic spins or defects, on the basis that at $T = 100 \text{ mK}$ and $B_0 = 1.5 \text{ T}$ any paramagnetic centre is highly polarized and its spin fluctuations exponentially suppressed. This constitutes the main difference between

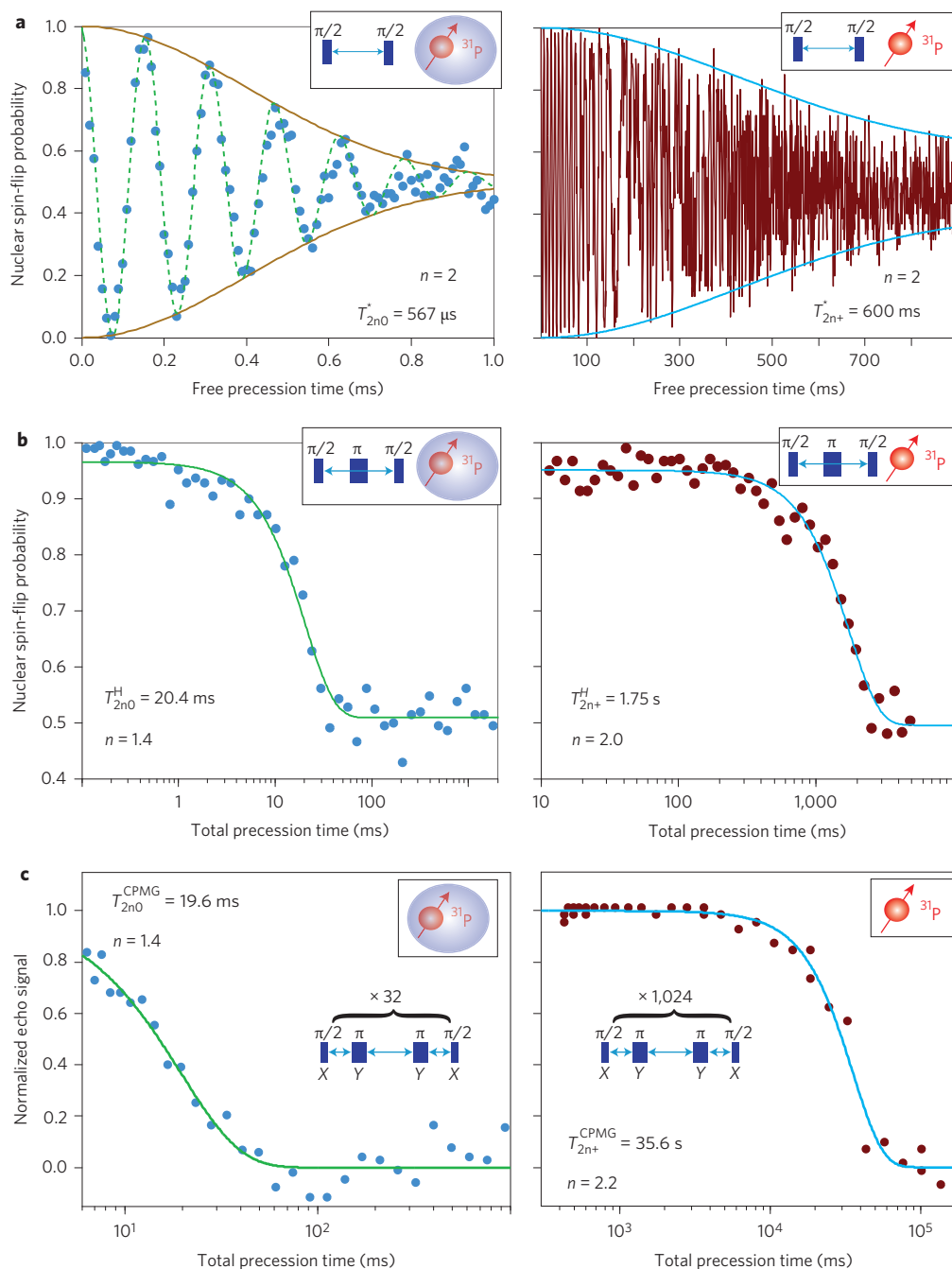


Figure 3 | Nuclear spin qubit. **a–c**, Nuclear spin coherence times obtained from Ramsey (**a**), Hahn-echo (**b**) and CPMG decay (**c**) measurements. Left column: neutral donor ($^{31}\text{P}^0$). Right column: ionized donor ($^{31}\text{P}^+$). For the CPMG sequences, the number of pairs of π -pulses is indicated in the insets. Fitting functions are of the form $P(t) = P_0 \exp(-(t/T_2)^n) + P_\infty$. All data are from device B. X and Y indicate the axes around which the spin is rotated, through the application of microwave pulses in-phase (X) or in-quadrature (Y) with the reference clock.

our work and earlier bulk experiments^{10,11} conducted at $T \approx 5$ K and $B_0 \approx 0.35$ T.

Second, we rule out decoherence from local charge noise, for example, two-level fluctuators at the Si/SiO₂ interface. We have verified that the e^- qubit is sensitive to electric field noise, by repeating the noise spectroscopy experiment in the presence of an oscillating voltage at 5 kHz, applied to an electrostatic gate above the qubit location (Supplementary Section F). This sensitivity could arise from a Stark shift of the hyperfine coupling¹⁴ or the g -factor¹⁵. However, the gate voltage amplitudes necessary to observe an effect in $S(\omega)$ are orders of magnitude larger than the charge noise we would expect in our device. Moreover, we have used the SET to measure the spectrum of the intrinsic charge

noise in the device (Supplementary Section F) and found it to follow a $1/\omega^\alpha$ dependence with $\alpha \approx 0.5$. This is in stark contrast with the measured spectrum of the noise acting on the qubit, where $\alpha = 2.5$.

We consider the most plausible source of low-frequency noise to be the instability of the external magnetic field B_0 produced by the superconducting solenoid. This would explain why the noise appears identical in both devices, because they were measured with the same cryomagnetic set-up. Also consistent with magnetic field noise is the fact that the ratio of the Hahn-echo times for the electron and bare nucleus, $T_{2n+}^H/T_{2e}^H = 1,636$ (device B), is very close to the ratio of the electron and nuclear magnetic dipoles, $\gamma_e/\gamma_n = 1,623$.

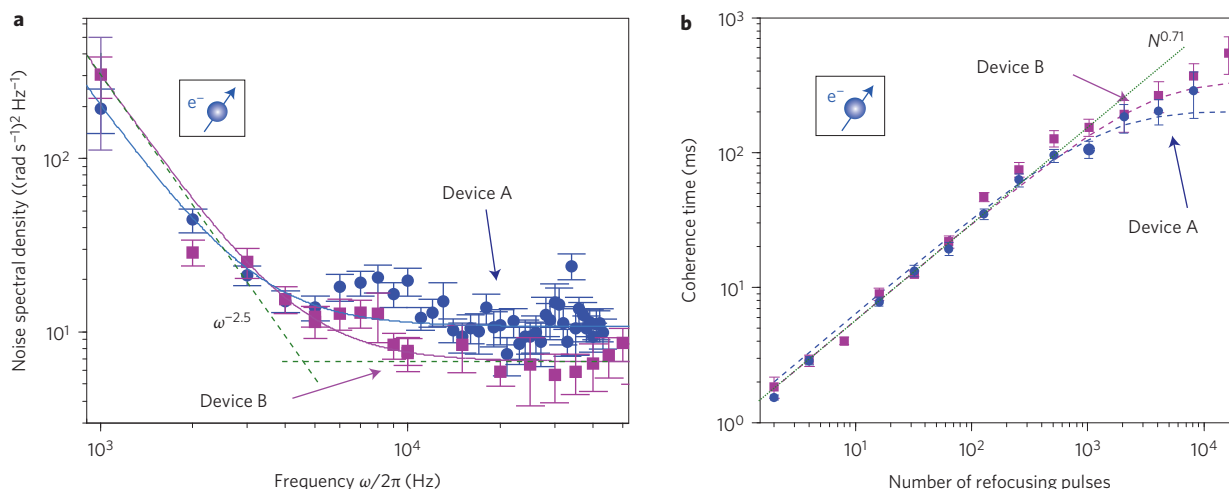


Figure 4 | Noise spectroscopy of the electron spin qubit. **a**, Noise power spectral densities ($S(\omega)$) for the electron spin qubit in device A (circles) and device B (squares). Solid lines are fits of the form $C_2/\omega^{2.5} + C_0$, with the following parameters: $C_2 = 6 \times 10^{11}$, $C_0 = 10$ for device A; $C_2 = 9 \times 10^{11}$, $C_0 = 6$ for device B. Dashed lines show the $C_2/\omega^{2.5}$ and C_0 terms separately for device B. **b**, Electron coherence times T_{2e}^{CPMG} from CPMG pulse sequences as a function of the number N of refocusing pulses. Dashed lines are theoretical predictions assuming the noise spectral density from the solid-line fits in **a**. The excellent agreement between the calculated lines and the data at low N proves that the $S(\omega) \propto \omega^{-2.5}$ dependence continues well below 1 kHz. With $S(\omega) \propto \omega^{-\alpha}$, the coherence time T_{2e}^{CPMG} is expected to scale as $N^{\alpha/(\alpha+1)}$ (ref. 28), yielding $N^{0.71}$ for $\alpha = 2.5$, which is shown in the figure as a guide to the eye (dotted line). Error bars are 95% confidence intervals from the exponential fits used to extract the decay times.

An extensive discussion of the plausibility of different noise sources is given in Supplementary Section F. With the data at hand we cannot make definitive statements about the residual decoherence mechanisms at play in our devices, but it appears likely that the electron qubit coherence is limited by thermal and magnetic noise external to the device. Conversely, device-intrinsic noise sources such as charge and spin fluctuators do not appear to play a role. Several engineering solutions can be applied to further reduce the influence of external noise and further improve the qubit coherence in future experiments.

Our results conclusively show that the exceptional quantum coherence exhibited by spins in isotopically pure ^{28}Si can be preserved and exploited in a top-gated nanoelectronic device, fabricated with standard metal–oxide–semiconductor methods. The proximity of an amorphous interface and gated nanostructures does not appear to significantly affect the control fidelities and the coherence times, which reach here a new record for solid-state single qubits with $T_2^{\text{CPMG}} > 30$ s in the $^{31}\text{P}^+$ spin. Looking beyond the single-qubit level, we note that the most promising proposals for 2-qubit logic gates and long-distance coupling involve rather weak interactions, either through exchange coupling²⁹, or in a circuit quantum electrodynamics (cQED) architecture³⁰. The extremely narrow linewidths observed here will facilitate multi-qubit operations based on magnetic resonance, because the individual resonances will remain resolvable over a very broad range of inter-qubit couplings, greatly relaxing the need for atomically precise donor placement. This work represents a fundamental advance in the control and understanding of spin qubits in the solid state and shows a clear path forward to integrating them with functional electronic devices.

Methods

Device fabrication. The device was fabricated on a 0.9- μm -thick epilayer of isotopically purified ^{28}Si , grown on top of a 500- μm -thick ^{nat}Si wafer. The ^{29}Si concentration was depleted to 800 ppm in the enriched ^{28}Si epilayer. Single-atom qubits were selected from a small group of donors implanted in a region adjacent the SET. In device A, individual P^+ atoms were ion-implanted at 14 keV energy in a $90 \times 90 \text{ nm}^2$ window defined by a resist mask. In device B, P_2^+ molecular ions were implanted at 20 keV energy, again in a $90 \times 90 \text{ nm}^2$ window. In both devices, an 8-nm-thick thermal SiO_2 oxide layer was grown on top of the Si wafer before nanofabrication and ion implantation. With the implantation energies used here, the

donors are expected to stop ~ 15 – 20 nm below the surface, thus ~ 10 nm below the Si/SiO_2 interface. All other nanofabrication processes were identical to those described in detail in ref. 21, except for a slight modification in the gate layout to bring the qubits closer to the microwave antenna and provide an expected factor 3 increase in B_1 for the same output power at the source.

Experimental set-up. The sample was mounted on a high-frequency printed circuit board in a copper enclosure, thermally anchored to the cold finger of an Oxford Kelvinox 100 dilution refrigerator with a base temperature of $T_{\text{bath}} = 20$ mK. The sample was placed in the centre of a wide-bore superconducting magnet, oriented so that the B_0 field was applied along the $[110]$ plane of the Si substrate and perpendicular to the short-circuit termination of the microwave antenna. The magnet was operated in persistent mode while also feeding the nominal current through the external leads. We found that removing the supply current while in persistent mode led to a very significant magnetic field and ESR frequency drift, unacceptable given the intrinsic sharpness of the resonance lines of our qubit. Conversely, opening the persistent mode switch led to noticeable deterioration of the spin coherence, most visible as a shortening of T_2^* in Ramsey experiments.

Room-temperature voltage noise was filtered using an anti-inductively wound coil of thin copper wire with a core of Eccosorb CRS-117 (~ 1 GHz cutoff), followed by two types of passive low-pass filter: 200 Hz second-order RC filters for d.c. biased lines and 80 MHz seventh-order Mini-Circuits LC filters for pulsed voltage lines. The filter assemblies were placed in copper enclosures, filled with copper powder, and thermally anchored to the mixing chamber. D.c. voltages were applied using optoisolated and battery-powered voltage sources, connected to the cold filter box via twisted-pair wires. Voltage pulses were applied using an arbitrary waveform generator (LeCroy ArbStudio 1104), connected to the filter box via semi-rigid coaxial lines.

ESR pulses were generated using an Agilent E8257D analogue signal generator, and NMR pulses were produced by an Agilent MXG N5182A vector signal generator. Both excitation signals were combined using a power combiner and fed to the microwave antenna via a CuNi semi-rigid coaxial cable, with attenuators at the 1.5 K stage (3 dB for device A, 10 dB for Device B) and the 20 mK stage (3 dB). The pulse and phase modulation of both microwave sources was controlled using a PCI TTL pulse generator (SpinCore PulseBlaster-ESR). The SET current was measured by a Femto DLPCA-200 transimpedance amplifier at room temperature, followed by a floating-input voltage post-amplifier, a sixth-order low-pass Bessel filter, and acquired using a PCI digitizer card (AlazarTech ATS9440).

Data acquisition statistics. For e^- experiments the state is always initialized spin-down and all of our plots were produced by taking the spin-up proportion from 100–200 single-shot measurement repetitions per point. For ^{31}P experiments, plots were produced by taking the nuclear flipping probability (no initialization to a certain state) from 41 measurement repetitions per point and 50 electron readouts per nuclear readout. See ref. 20 for more details on nuclear readout and control sequences.

Received 28 February 2014; accepted 22 August 2014;
published online 12 October 2014

References

1. Awschalom, D. D., Bassett, L. C., Dzurak, A. S., Hu, E. L. & Petta, J. R. Quantum spintronics: engineering and manipulating atom-like spins in semiconductors. *Science* **339**, 1174–1179 (2013).
2. Zwanenburg, F. A. *et al.* Silicon quantum electronics. *Rev. Mod. Phys.* **85**, 961–1019 (2013).
3. Yao, W., Liu, R.-B. & Sham, L. Theory of electron spin decoherence by interacting nuclear spins in a quantum dot. *Phys. Rev. B* **74**, 195301 (2006).
4. De Sousa, R. Dangling-bond spin relaxation and magnetic $1/f$ noise from the amorphous-semiconductor/oxide interface: theory. *Phys. Rev. B* **76**, 245306 (2007).
5. Witzel, W. M., Carroll, M. S., Morello, A., Cywinski, L. & Das Sarma, S. Electron spin decoherence in isotope-enriched silicon. *Phys. Rev. Lett.* **105**, 187602 (2010).
6. Tyryshkin, A. M. *et al.* Electron spin coherence exceeding seconds in high-purity silicon. *Nature Mater.* **11**, 143–147 (2012).
7. Steger, M. *et al.* Quantum information storage for over 180 s using donor spins in a ^{28}Si 'semiconductor vacuum'. *Science* **336**, 1280–1283 (2012).
8. Saeedi, K. *et al.* Room-temperature quantum bit storage exceeding 39 minutes using ionized donors in silicon-28. *Science* **342**, 830–833 (2013).
9. Alvarez, G. A. & Suter, D. Measuring the spectrum of colored noise by dynamical decoupling. *Phys. Rev. Lett.* **107**, 230501 (2011).
10. Schenkel, T. *et al.* Electrical activation and electron spin coherence of ultralow dose antimony implants in silicon. *Appl. Phys. Lett.* **88**, 112101 (2006).
11. Paik, S.-Y., Lee, S.-Y., Baker, W., McCamey, D. & Boehme, C. t_1 and t_2 spin relaxation time limitations of phosphorous donor electrons near crystalline silicon to silicon dioxide interface defects. *Phys. Rev. B* **81**, 075214 (2010).
12. Wolfowicz, G. *et al.* Atomic clock transitions in silicon-based spin qubits. *Nature Nanotech.* **8**, 561–564 (2013).
13. Laird, E. A., Pei, F. & Kouwenhoven, L. A valley-spin qubit in a carbon nanotube. *Nature Nanotech.* **8**, 565–568 (2013).
14. Mohiyaddin, F. A. *et al.* Noninvasive spatial metrology of single-atom devices. *Nano Lett.* **13**, 1903–1909 (2013).
15. Rahman, R., Park, S. H., Boykin, T. B., Klimeck, G., Rogge, S. & Hollenberg, L. C. L. Gate-induced g -factor control and dimensional transition for donors in multivalley semiconductors. *Phys. Rev. B* **80**, 155301 (2009).
16. Greenland, P. *et al.* Coherent control of Rydberg states in silicon. *Nature* **465**, 1057–1061 (2010).
17. Morello, A. *et al.* Single-shot readout of an electron spin in silicon. *Nature* **467**, 687–691 (2010).
18. Dehollain, J. P., Pla, J. J., Siew, E., Tan, K. Y., Dzurak, A. S. & Morello, A. Nanoscale broadband transmission lines for spin qubit control. *Nanotechnology* **24**, 015202 (2013).
19. Jamieson, D. N. *et al.* Controlled shallow single-ion implantation in silicon using an active substrate for sub-20-keV ions. *Appl. Phys. Lett.* **86**, 202101 (2005).
20. Pla, J. J. *et al.* High-fidelity readout and control of a nuclear spin qubit in silicon. *Nature* **496**, 334–338 (2013).
21. Pla, J. J. *et al.* A single-atom electron spin qubit in silicon. *Nature* **489**, 541–545 (2012).
22. Balasubramanian, G. *et al.* Ultralong spin coherence time in isotopically engineered diamond. *Nature Mater.* **8**, 383–387 (2009).
23. Maurer, P. C. *et al.* Room-temperature quantum bit memory exceeding one second. *Science* **336**, 1283–1286 (2012).
24. Morton, J. J. L. *et al.* Measuring errors in single-qubit rotations by pulsed electron paramagnetic resonance. *Phys. Rev. A* **71**, 012332 (2005).
25. Cywinski, L., Lutchyn, R. M., Nave, C. P. & Das Sarma, S. How to enhance dephasing time in superconducting qubits. *Phys. Rev. B* **77**, 174509 (2008).
26. Bylander, J. *et al.* Noise spectroscopy through dynamical decoupling with a superconducting flux qubit. *Nature Phys.* **7**, 565–570 (2011).
27. Taylor, J. *et al.* High-sensitivity diamond magnetometer with nanoscale resolution. *Nature Phys.* **4**, 810–816 (2008).
28. Medford, J. *et al.* Scaling of dynamical decoupling for spin qubits. *Phys. Rev. Lett.* **108**, 086802 (2012).
29. Kalra, R., Laucht, A., Hill, C. D. & Morello, A. Robust two-qubit gates for donors in silicon controlled by hyperfine interactions. *Phys. Rev. X* **4**, 021044 (2014).
30. Hu, X., Liu, Y.-X. & Nori, F. Strong coupling of a spin qubit to a superconducting stripline cavity. *Phys. Rev. B* **86**, 035314 (2012).

Acknowledgements

The authors thank M.J. Biercuk for discussions. This research was funded by the Australian Research Council Centre of Excellence for Quantum Computation and Communication Technology (project no. CE11E0001027) and the US Army Research Office (W911NF-13-1-0024). The authors acknowledge support from the Australian National Fabrication Facility and from the laboratory of Robert Elliman at the Australian National University for ion implantation facilities. The work at Keio has been supported in part by FIRST, the Core-to-Core Program by JSPS and the Grant-in-Aid for Scientific Research and Project for Developing Innovation Systems by MEXT.

Author contributions

J.T.M., J.P.D., A.S.D. and A.M. designed the experiments. J.T.M., J.P.D. and A.L. performed the measurements and analysed the results with A.M.'s supervision. D.N.J. and J.C.M. designed the P implantation experiments. F.E.H. fabricated the device with A.S.D.'s supervision and R.K.'s assistance. T.S. and K.M.I. prepared and supplied the ^{28}Si epilayer wafer. J.T.M., J.P.D. and A.M. wrote the manuscript, with input from all co-authors.

Additional information

Supplementary information is available in the [online version](#) of the paper. Reprints and permissions information is available online at www.nature.com/reprints. Correspondence and requests for materials should be addressed to J.T.M. and A.M.

Competing financial interests

The authors declare no competing financial interests.